Modeling and Analysis of Magnetic Field Induced Coupling on Embedded STT-MRAM Arrays

Insik Yoon, *Student Member, IEEE*, and Arijit Raychowdhury, *Senior Member, IEEE*

Abstract—Spin transfer torque magnetic random access memory (STT-MRAM) is an emerging memory technology which exhibits nonvolatility, high density, high endurance, and nanosecond read and write times. These characteristics make STT-MRAM suitable for last-level cache and other embedded applications. The STT-MRAM bit-cell consists of a magnetic tunnel junction (MTJ) which is composed of two ferromagnetic layers (free and fixed layers) and one insulating layer in between. As STT-MRAM arrays become denser to meet cost and requirements of high performance computing, the distance between adjacent MTJ bits reduces. This aggravates the magnetic coupling from free and fixed layer of one MTJ bit to its neighbors. Even though magnetic coupling is expected to become stronger as MTJ scales down, its impacts on static and dynamic properties on MTJ is relatively unexplored. In this paper, we present a model of the magnetic field coupling in high-density MTJ arrays for three different types of MTJ stacks and evaluate the effect of magnetic field induced coupling on static and dynamic properties. Lastly, we show how process induced variations in MTJ characteristics affect the magnitude of magnetic coupling and their effect on the electrical characteristics of the STT-RAM arrays.

Index Terms—Embedded memory, magnetic coupling, magnetic field, spin transfer torque magnetic random access memory (STT-MRAM).

I. INTRODUCTION

AN SPIN transfer torque magnetic random access memory (STT-MRAM) bit-cell consists of one access transistor and one magnetic tunnel junction (MTJ). The data is stored in MTJ [1]. Typical MTJ stacks comprise of an insulator (MgO) which is sandwiched between a fixed ferromagnetic layer (typically CoFeB-based) whose magnetic moment is pinned to one direction and a "free" ferromagnetic layer whose moment changes direction based on applied external current or magnetic field. Since MTJ exhibits tunneling magnetoresistance [2], the resistance of the stack changes depending on the orientation of the free layer, which in turn stored the data of the bit-cell. When the direction of the magnetic moment inside the free layer of an MTJ is anti-parallel to the fixed layer, the

MTJ has high resistance and its state is defined as bit "1" [1]. Likewise, when the direction of the magnetic moment in an MTJ is parallel to the magnetic moment of the fixed layer, the MTJ exhibits low resistance and it is defined as bit "0." The write operation is performed by passing spin-polarized current through the fixed or free layer and it polarizes the current in its preferred direction of magnetic moment. The spin-polarized current exerts a torque on the free layer and causes it to change its direction of magnetic moment. This results in a bit-flip and a successful write operation. The read operation comprises of passing a weak current through the bit and sensing the resistive state of the MTJ stack. As STT-MRAM arrays become dense and the cell dimensions become smaller, the magnetic field coupling from ferromagnetic layers of one MTJs affect write and read operation of its neighboring bits. As shown in [3], scaling MTJ in a densely packed array causes program errors due to large stray field coupling. When MTJ scales down and they are densely packed in an array, magnetic coupling of MTJs could become a significant problem since the distance of the ferromagnets, free and fixed layer of MTJs, reduces to cause even stronger magnetic coupling. Therefore, there is an urgent need to identify how magnetic coupling affects properties of STT-MRAM and analyze whether magnetic coupling will pose as a scaling challenge in further scaling of STT-MRAM dimensions.

There is limited prior work on the analysis of magnetic coupling on STT-MRAM arrays. Observation of H_{stray} in victim MTJ with four neighboring MTJs in technology scaling was presented by one of the authors in [4]. However, detailed models of magnetic coupling, the role of technology scaling on stray field and their effect on the electrical characteristics has not been discussed. On the other hand, there is ample research that analyzes how static and dynamic properties of MTJ are affected by technology scaling. Chun *et al.* [5] and Chen *et al.* [6] presented a scaling roadmap of MTJ that contains trends for thermal stability, switching current density (J_{c0}), critical switching current (I_c), resistance-area product, etc. The effect of technology scaling on the dynamic properties of MTJs is also well explored; [7] and [8] present how write current (I_c) and critical current density (J_{c0}) change with technology nodes. While scaling MTJ dimension, the authors calibrate H_k to maintain a target thermal stability of the MTJ. Chen *et al.* [9] presented changes in write current density (J_{c0}) across different MTJ types. Further, [10], [11] proposes a scaling trend of anisotropy energy ($K_u t$) for single and dual interface MTJs. The authors also present models of thermal stability as a functions of MTJ dimensions.

The authors are with the School of Electrical and Computer Engineering, Georgia Institute of Technology, Atlanta, GA 30332 USA (e-mail: iyoon@gatech.edu; arijit.raychowdhury@ece.gatech.edu).
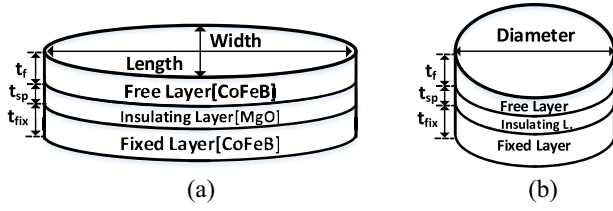
Fig. 1. (a) IMTJ. (b) PMTJ physical dimensions of MTJ cell types. The PMTJ can be bulk or interface PMTJ.

TABLE I
PHYSICAL DIMENSIONS OF MTJ IN STT-MRAM BIT-CELLS
ACROSS TECHNOLOGY GENERATIONS

Cell type	Dimension Parameter(nm)	Technology node(nm)			
		22nm	16nm	10nm	7nm
IMTJ	width	50	35	24.5	17.2
	length	AR*width			
	t_f	3			
	t_{fix}	5			
	t_{sp}	1.2			
Bulk PMTJ	diameter	40	28	19.6	13.7
	t_f	3			
	t_{fix}	5			
	t_{sp}	1.2			
Interface PMTJ	diameter	40	28	19.6	13.7
	t_f	variable dependent on delta			
	t_{fix}	3			
	t_{sp}	0.9			

Fig. 2. Schematic representation of current loops in the nanomagnet.

Raychowdhury *et al.* [12] examined how P_{fail} of a chip, which relates to thermal stability, changes with technology node. We also explore the case where the fixed layer is an anti-ferromagnet and the magnetic fields are closed. In this case, the free layer nanomagnets create the magnetic field which affects the performance and stability of the victim cell.

In this paper, we analyze how magnetic coupling affects both static and dynamic properties of MTJs with in-plane anisotropy [13], bulk perpendicular anisotropy [14], and interface induced perpendicular anisotropy [15] across different technology nodes. In Section II, we present a compact model of MTJs and show the effect of magnetic field coupling as a function of MTJ dimensions and spacings. In Section III, the data pattern dependence of magnetic coupling is analyzed in a 3×3 array and the worst case data pattern for each of the MTJ stacks is discussed. Sections IV and V present how static properties (Δ, τ) and dynamic properties (J_{c0}, t_{wr}) are affected by different scenarios of magnetic field induced coupling. Lastly, sensitivity analysis is performed in Section VI to show how process induced variation that directly impact magnetic coupling affect both static and dynamic properties of MTJs.

II. MODELING

A. MTJ Physical Dimension Modeling

From [14] and [16], dimensions of in-plane, bulk and interface-induced perpendicular MTJ (PMTJ) are retrieved. For more details on the three types on MTJs and their relative merits/demerits and role in the technology development, interested readers are pointed to [4] and [17]–[19]. in-plane MTJ (IMTJ) is modeled as an elliptical pillar and PMTJ are modeled as cylinders.

Fig. 1 illustrates the physical dimensions of in-plane and PMTJ cells. In Fig. 1 t_f, t_{sp}, and t_{fix} represent thickness of free layer, insulating layer, and fixed layer, respectively. Length of IMTJ is determined by the product of aspect ratio (AR) and the width of the IMTJ. Since AR is one of the factors that determines H_k and thermal stability, its value changes with target thermal stability. In order to observe how magnetic coupling of MTJ cell array change with respect to technology node, we scale physical dimensions of MTJs. Table I shows physical dimensions at different technology node. Saturation magnetization remains constant in all the technology nodes. Similar to AR in IMTJ, free layer thickness (t_f) of interface PMTJ is also an important design variable that determines thermal stability. Therefore, AR and t_f are scaled appropriately

to maintain a constant thermal stability in all the technology nodes. From [7] and [14], device parameters of Table I were chosen.

B. Modeling the H Field

The magnetic field of a single MTJ is first modeled to observe the net magnetic field coupling between adjacent cells. In an STT-MRAM array we consider a cell in the center of a 3×3 lattice as the victim cell and the eight neighbors as aggressors. Under the assumption of uniform magnetization of the MTJ material, the magnetic dipoles inside MTJs cancel out and finally the magnetic dipoles on the edges of the MTJ are unpaired.

Magnetic dipoles can be in turn modeled as current loops following [20]. Fig. 2 shows how magnetic dipoles inside an MTJ cancels each other's internal current loops [20]. Hence, we model an MTJ as a solenoid which has bound current paths wrapped around itself to produce the saturation magnetization (M_s) of an MTJ as described in [14].

Since magnetic moment is derived from the volume and M_s of an MTJ [$M_s = (Magnetic\ moment/Volume\ of\ MTJ)$] and it is the product of the bound current, the cross sectional area of the MTJ, and the number of coils, the amount of current needed to produce the magnetic field can be calculated. The current is expressed as ($M_s t/no.\ of\ coils$), t is the thickness of an MTJ layer.

Fig. 3 shows the IMTJ and PMTJ with the corresponding solenoid model for evaluating the resultant magnetic field. The current loop around an MTJ is wrapped around in a direction that generates the net M_s. Finally, we can calculate the
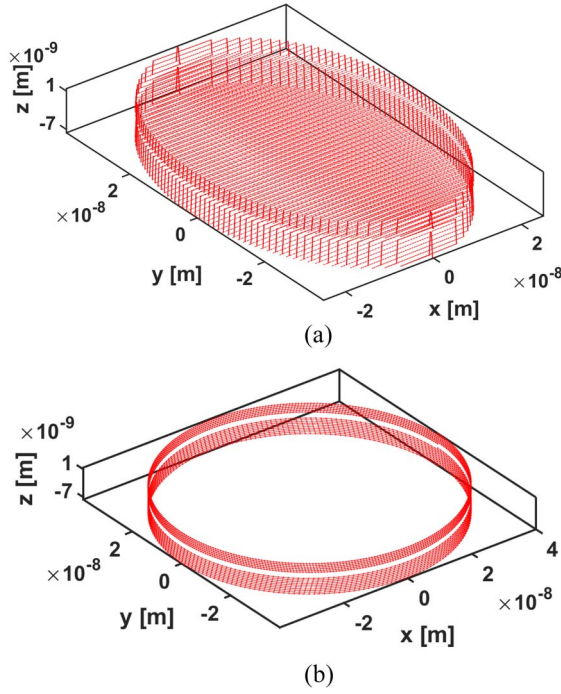
Fig. 3. Solenoid representation of current loops in IMTJ and PMTJ to model magnetic field around MTJs. Solenoid modeling of free and fixed layer of (a) IMTJ and (b) PMTJ.
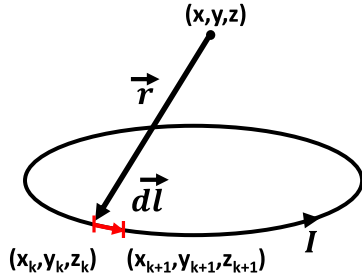

Fig. 4. Finite element representation of Biot–Savart law.

magnetic field at any specific point in space by applying the Biot–Savart law [20], as

$$\vec{H}(x, y, z) = \frac{I}{4\pi} \int_C \frac{d\vec{l} \times \vec{r}}{|\vec{r}|^3} \tag{1}$$

where, $d\vec{l}$ is defined by $\{d\vec{x}, d\vec{y}, d\vec{z}\}$, which is equal to $\{\vec{x}_{k+1} - \vec{x}_k, \vec{y}_{k+1} - \vec{y}_k, \vec{z}_{k+1} - \vec{z}_k\}$ from Fig. 4.

Algorithm 1 shows the pseudo-code for a discrete finite element representation of Biot–Savart law, which is used to calculate magnetic field at coordinate (x, y, z). For each segment in the model, Algorithm 1 computes dHx, dHy, and dHz, x, y, z components of $d\vec{l} \times \vec{r}$, and stores it in an array. After computing $d\vec{l} \times \vec{r}$ for all segments, we can find the magnetic field in x, y, and z direction at point (x, y, z) by summing up dHx, dHy, and dHz and multiplying by the coefficient $(I/4\pi)$.

By using Biot–Savart law and finite element method as above, we find magnetic field at a set of coordinates in 3-D space and Fig. 5 shows the complete magnetic field modeling for free layer of IMTJ and PMTJ in space. In Fig. 5, The magnetic field direction between Fig. 5(a)–(d) are opposite to

---

Algorithm 1: Biot–Savart Law for Finding Magnetic Field H at (x, y, z) Coordinate

Result: Calculate H_{stray} from MTJs at coordinate (x,y,z)
N = number of points in MTJ model;
$x_p[N]$ = array of x-coordinates of MTJ model;
$y_p[N]$ = array of y-coordinates of MTJ model;
$z_p[N]$ = array of z-coordinates of MTJ model;
for $k = 1; k < N - 1; k + +$ **do**
  r_mag = sqrt(($x - x_p[k])^2 + (y - y_p[k])^2 + (z - z_p[k])^2$);
  dx[k] = $x_p[k + 1] - x_p[k]$;
  dy[k] = $y_p[k + 1] - y_p[k]$;
  dz[k] = $z_p[k + 1] - z_p[k]$;
  dHx[k] = (dy[k] * (z - $z_p[k]$) - dz[k] * (y - $y_p[k]$))/(r_mag)^3;
  dHy[k] = (dz[k] * (x - $x_p[k]$) - dx[k] * (z - $z_p[k]$))/(r_mag)^3;
  dHz[k] = (dx[k] * (y - $y_p[k]$) - dy[k] * (x - $x_p[k]$))/(r_mag)^3;
end
Hx = (I/(4*pi))*sum(dHx);
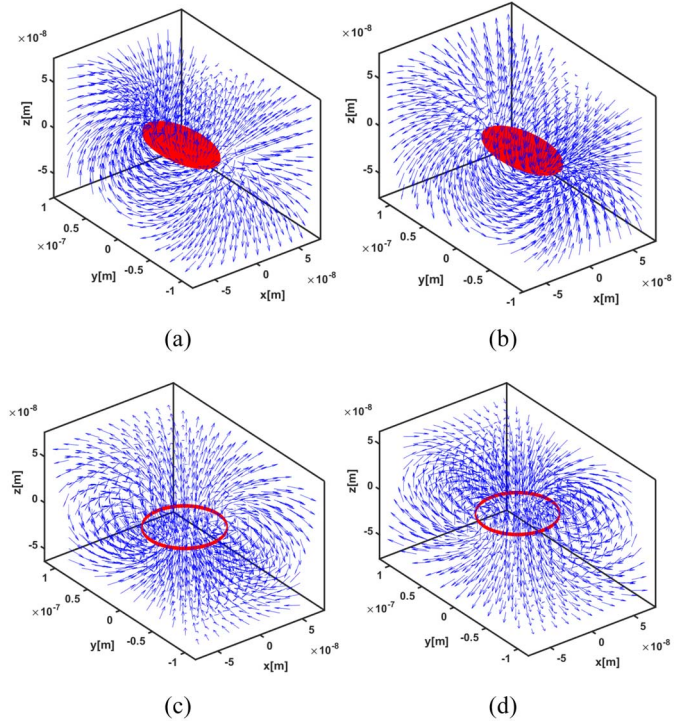Hy = (I/(4*pi))*sum(dHy);
Hz = (I/(4*pi))*sum(dHz);

Fig. 5. Magnetic field around IMTJ and PMTJ when current is applied to current loops. Current flowing from (a) $+y$ to $-y$ direction, (b) $-y$ to $+y$ direction, (c) $-z$ to $+z$ direction, and (d) $+z$ to $-z$ direction.

each other because direction of bound current into the coil is opposite.

We expect that the magnetic coupling between aggressor cells and a victim cell would be affected by the distance between the cells 1. In order to observe the difference in $\vec{H}$ with respect to distance between cells, we consider two types of MTJ cells: 1) a nominal cell of size $5F \times 3F$ and 2) a compact cell size as $3F \times 2F$. Here F is the half-pitch of the poly silicon layer for a given technology node.

Fig. 6 shows the nominal and compact cells in array configurations. The MTJ at the center of an array in Fig. 6 is the victim MTJ and distance labeled in Fig. 6 is the center to center distance between the victim cell and its aggressor

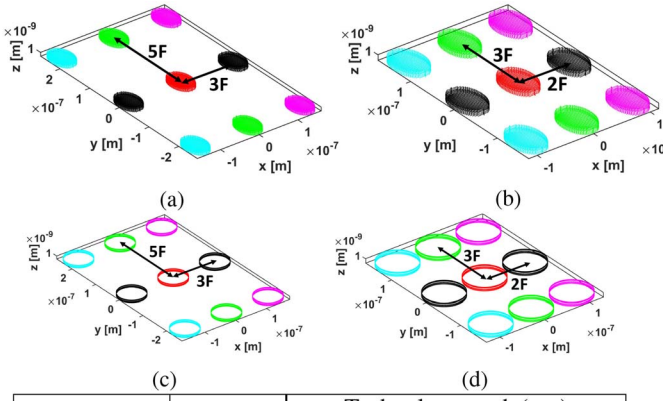| spacing(nm)	cell size	Technology node(nm)			
		22nm	16nm	10nm	7nm
x-spacing	normal	135	96	60	42
	compact	90	64	40	28
y-spacing	normal	225	160	100	70
	compact	135	96	60	42

Fig. 6. IMTJ (a) default cell array and (b) compact cell array. PMTJ (c) normal default array and (d) compact cell array.
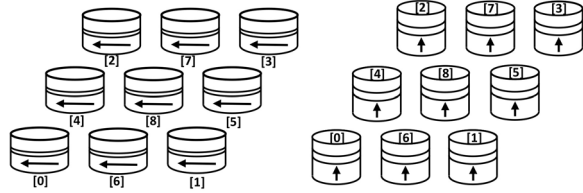

Fig. 7. Arrangement of MTJs in a 3 × 3 array [23].

neighboring cells. For each cell, we model the net magnetic field generated by both the free layer and the fixed layers. Then we calculate the net magnetic field from each MTJ and compute the total magnetic field at the victim node. Although the fixed layer has its magnetic moment pointing in a specific direction, the direction of the magnetic moment in the free layer is data dependent. Hence, the net field generated by the neighboring cells on the victim, depends on the overall data pattern of the 3 × 3 array. In the next section, we explore the effect of data pattern on the coupling field on the victim node and determine the worst and best data patterns that can reduce magnetic coupling. It should be noted that our discussion in this paper is limited to the nanomagnet. The access transistor in the bit-cell plays an important role in the cell dynamics [21], [22], especially the write properties. The retention properties of the cell are not disturbed by the access transistor, at least to the first order. However, the aim of this paper is to explore the performance and retention behavior of bit-cells with and without magnetic coupling from the neighboring cells. Hence, we have not considered the role of the access transistor in our discussions.

III. ROLE OF MAGNETIC COUPLING IN DENSE ARRAYS

Similar to electrical coupling between dynamic random access memory cells [24], the data pattern on neighboring STT-MRAM cells can cause magnetic coupling with a cell
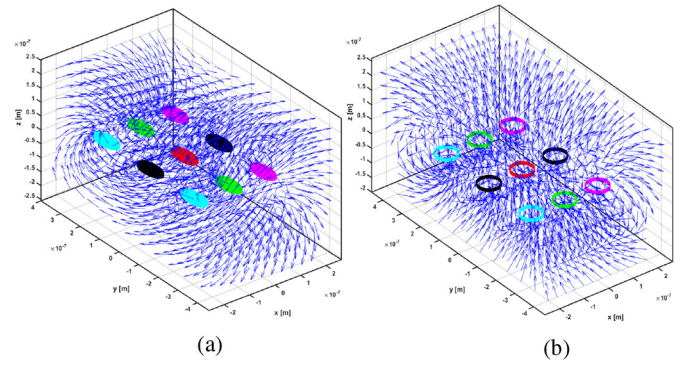

Fig. 8. Magnetic field visualization of IMTJ and PMTJ 3 × 3 arrays for the worst data pattern [23]. (a) IMTJ. (b) PMTJ.

since data inside a nanomagnet determines magnetic field direction. we need to analyze the magnetic field coupling and its magnitude in STT-MRAM bitcells. In this section, we present modeling of magnetic coupling effects on a 3 × 3 array and analyze the best case and worst case data patterns which yields minimum and maximum magnetic coupling on a cell at the center of the array. In order to capture the complete magnetic coupling effect from adjacent cells, doing analysis with more number of adjacent cells can increase the accuracy of the model. However, since magnetic field decreases quadratically with distance, the cells that are farther away would assert a very weak field on the victim. Hence, we invoke the near neighbor interactions only, which is staple in the modeling and simulation of most interacting magnetic structures. We increase the accuracy of our model by including the diagonal elements as opposed to only the four nearest neighbors. Therefore, we use a nine cell lattice, to explore how magnetic coupling affects the victim cell's characteristics.

Initial results and observations on the data pattern dependence of magnetic coupling have been briefly discussed by Yoon *et al.* [23]. The magnetic coupling is measured by adding magnetic field vectors from neighboring nanomagnets on the victim cell. Fig. 7 shows the arrangements of the 3 × 3 array of magnets and the figure denotes that victim bit is located at position [8]. Fig. 8 shows the magnetic field from IMTJ and PMTJ arrays which saturation magnetization is set to 1.257e6 A/m.

A. Impact of Magnetic Coupling on Write and Retention

To visualize the best and worst case data patterns, we represent the information stored in the 3 × 3 array as a 9-bit number where each bit represents the data stored (0 for antiparallel and 1 for parallel) in the *i*th bit as shown in Fig. 7. Because of this encoding, data patterns 0 to 255 represent the victim storing a 0 and 256 to 511 represents the victim storing a 1. Fig. 9 show residual magnetic field strength from all the aggressors for all possible data arrangements. Residual field in the direction of the free layer's magnetization enhances stability and improves retention (thereby degrading writability) while residual fields in the opposite direction would tend to destabilize the magnet. From Fig. 11, we note that data patterns [111 000 000] and [011 000 000] are the best and worst case data patterns for thermal stability (or retention) for IMTJ.
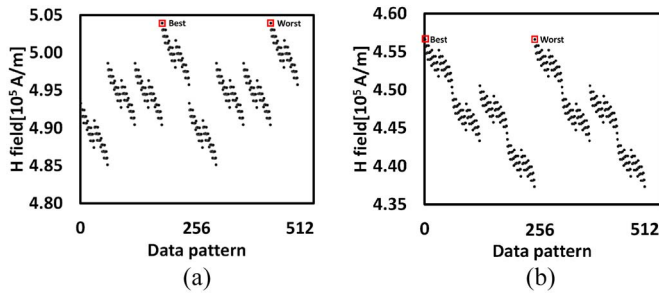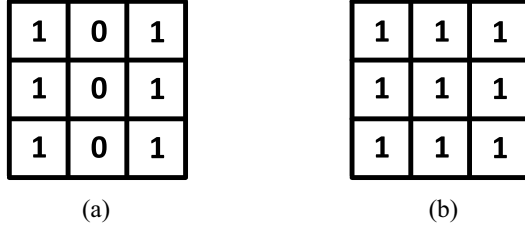
Fig. 9. Residual H field versus data pattern in (a) IMTJ and (b) PMTJ [23].

Fig. 10. Magnetic coupling induced worst-case data pattern for thermal stability [23]. (a) IMTJ block data pattern. (b) PMTJ block data pattern.

For both varieties of PMTJ, best and worst data patterns are [100 000 000] and [000 000 000]. The residual field is taken at the center of free layer of a victim cell.

Due to the uni-axial anisotropy in two MTJ types, best and worst case data pattern are different between in-plane and PMTJs, i.e., due to their physical structure and anisotropy. While the magnetization of IMTJ is aligned to the y-axis and magnetization in PMTJs is aligned to the z-axis. Therefore, the best and worst case data pattern for IMTJ and PMTJ are different as the vector field on the victim magnet and its effect on the victim need to be evaluated.

The worst case patterns for the 3×3 block is shown in Fig. 10.

IV. EFFECT OF MAGNETIC COUPLING ON STATIC CHARACTERISTICS OF THE VICTIM CELL

In static analysis, we analyze the effect of magnetic coupling on thermal stability and retention of a victim cell, i.e., the cell at the center of the 3×3 STT-MRAM array. Analysis is conducted on in-plane (IMTJ), bulk and interface-induced PMTJs (crystal (bulk) perpendicular magnetic tunnel junction (CPMTJ), interface-induced perpendicular magnetic tunnel junction (IPMTJ)). By varying the technology nodes (22/16/10/7 nm), we observe how change in physical dimension of an MTJ and the distance between MTJs in 3×3 array impact the magnetic coupling and its effect on Δ and retention. Also, effect of cell size (nominalcompact) and bestworst data patterns on magnetic coupling in each MTJ types is studied. In order to gauge how magnetic coupling causes variation with respect to Δ, we set nominal Δ of MTJs to be 20, 40, and 60. These three types of MTJs represent tradeoffs between nonvolatility and lower write power [25]. In short, we analyze the following.

1) Which type of MTJ is affected the most from magnetic coupling in terms of thermal stability and retention.
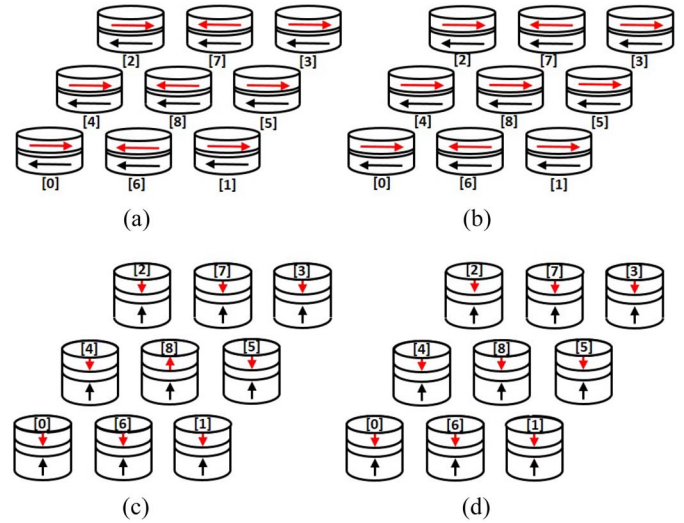

Fig. 11. MTJ best/worst data pattern [23]. (a) Best case [000 111 111]. (b) Worst case [100 111 111]. (c) Best case [011 111 111]. (d) Worst case [111 111 111].

2) The effect of magnetic coupling on thermal stability and retention with respect to changes in:
   a) target thermal stability ($\Delta = 20, 40, 60$);
   b) technology scaling (22/16/10/7 nm);
   c) nominal and compact cell sizes (15 F^2 versus 6 F^2);
   d) best/worst data pattern.

Based on M_s (1.257e6 A/m) and physical dimension of MTJs discussed in Table I, we modify other parameters of MTJs to set nominal Δ of MTJ to be 20, 40, and 60. Since Δ is defined as [26]

$$\Delta = \frac{K_u V}{k_B T} = \frac{H_k M_s V}{2 k_B T} \tag{2}$$

we vary H_k to achieve nominal Δ. However, since H_k is a property which is related to AR, K_u, and t_f in IMTJ, CPTMJ, and IPTMJ according to

$$\text{IMTJ } H_k = 2\left(\frac{4\pi M_s t(\text{AR} - 1)}{w\text{AR}}\right). \tag{3}$$

Reference [16]

$$\text{Bulk PMTJ } H_k = \frac{2K_u}{M_s} - 4\pi M_s. \tag{4}$$

Reference [26]

$$\text{Interfacial PMTJ } H_k = \frac{4\pi M_s^2 t_c}{M_s t_f} - 4\pi N_{DZ} M_s. \tag{5}$$

Reference [7] t_c from (5) is critical thickness of CoFeB layer. N_{DZ} is z-axis dependent demagnetizing factor. Since AR and t_f both affect H_k and volume of MTJ, they are determined through iterations between H_k and Δ (2), (3), and (5). AR, K_u, and t_f parameters for different nominal Δ in technology nodes are defined in Table II.

TABLE II
DESIGN PARAMETERS FOR MAINTAINING A TARGET Δ

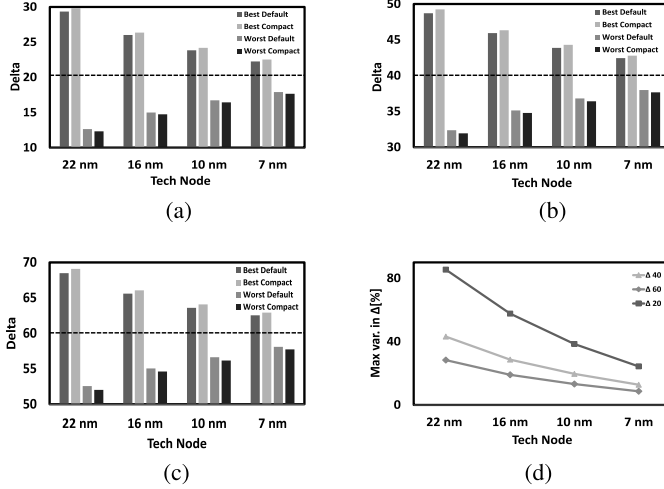| Cell type	Variable properties	Δ @85C	Technology node(nm)			
			22	16	10	7
IMTJ	Aspect Ratio	20	1.147	1.21	1.3	1.425
		40	1.293	1.421	1.6	1.853
		60	1.44	1.628	1.895	2.28
Bulk PMTJ	K_u (10^6J/m^3)	20	0.909	0.936	0.992	1.106
		40	0.935	0.989	1.101	1.329
		60	0.961	1.043	1.21	1.553
Interface PMTJ	t_f (nm)	20	1.485	1.471	1.441	1.379
		40	1.471	1.442	1.382	1.258
		60	1.457	1.413	1.323	1.137

Fig. 12. Variation of Δ in IMTJ with respect to technology nodes, data patterns and cell array configuration. Variation with nominal (a) $\Delta = 20$, (b) $\Delta = 40$, and (c) $\Delta = 60$. (d) Maximum variation of Δ across combinations of data pattern and cell array configuration in technology node.

Fig. 13. Variation of H_{stray}/H_k in IMTJ with respect to technology nodes, data patterns, and cell array configuration. Variation with nominal (a) $\Delta = 20$, (b) $\Delta = 40$, and (c) $\Delta = 60$. (d) Maximum variation of H_{stray}/H_k across combinations of data pattern and cell array configuration in technology node.

A. Effect of Magnetic Coupling on Thermal Stability

The effect of magnetic field on the stored magnetic energy in an MTJ can be modeled as [16]

$$\Delta(H) = \Delta(H = 0)\left(1 \pm \frac{H_{\text{stray}}}{H_k}\right)^2. \tag{6}$$

This shows that an external magnetic field (normalized by H_k) at the free layer of victim cell can cause variation in Δ of MTJ. We model the magnetic field from neighboring cells and the vector field, (H_{stray}) is calculated and it is applied to the victim cell as shown in (6).

1) In-Plane MTJ: Fig. 12 represents the variation of Δ in an IMTJ due to H_{stray} with respect to technology node, cell size, and data pattern for target $\Delta = 20/40/60$. Dotted line in the figure represents target Δ. The data patterns in MTJ array that yield the H parallel and anti-parallel to magnetization of victim cell are labeled as best and worst in the figure. The labels nominal and compact indicate the nominal and compact cell sizes as defined in earlier sections.

The common trend in Δ variation in Fig. 12 is that the variation is decreasing as we decrease technology node. This phenomenon is expected because as we decrease technology node, the volume of MTJ is decreasing and it causes Δ to decrease (2). In order to maintain target Δ across all technology nodes, we can either adjust M_s or H_k. In this analysis, we fixed M_s to be constant for all technology nodes, as it is
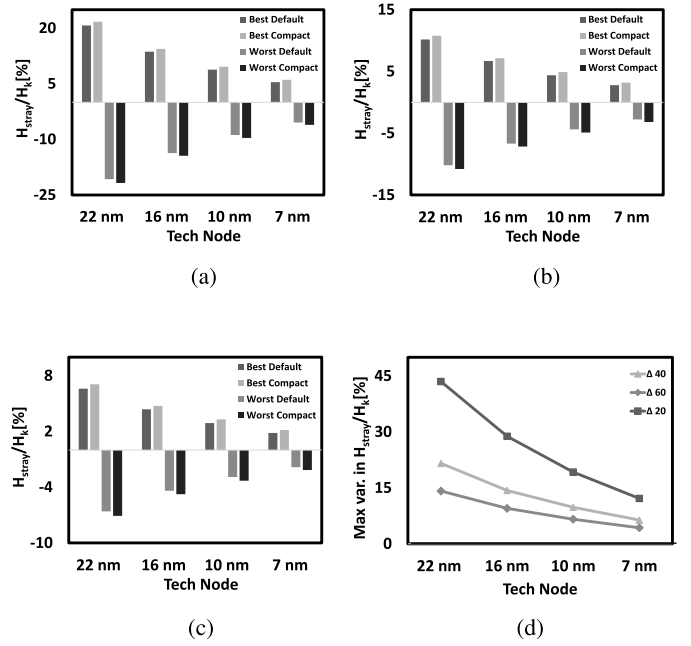
a material property. We tune geometric parameters of the bit cell to achieve a target H_k. Hence, with technology scaling, the magnetic coupling does increase, but surprisingly we note that a stronger cell anisotropy (owing to increased H_k), results in an effective decrease of H_{stray}/H_k. Fig. 13 shows the variation of (H_{stray}/H_k) across technology nodes. (H_{stray}/H_k) is positive when H_{stray} is aligned with M_s and negative when it is anti-parallel to M_s. As we can see, (H_{stray}/H_k) is decreasing as technology scales. The second trend that we observe from Fig. 12(d) is that the maximum variation (%) across data pattern and cell size decreases as target Δ changes from 20 to 60. This is due to increasing in H_k as target Δ increases. With same M_s, the only variable to tune Δ of an MTJ to target Δ is H_k. Therefore, H_k increases as target Δ increases. As we discussed in Section III, best data pattern, which causes maximum H_{stray} in direction of M_s, boosts Δ and the worst data pattern that causes maximum H_{stray} in the opposite direction of M_s degrades Δ. When it couples with cell size, it yields maximum variation of 85% between a compact cell with best data pattern and a compact cell with worst data pattern when target $\Delta = 20$ in 22 nm based on 12(d). On the other hand, at target $\Delta = 60$ in 7 nm, the maximum variation between compact cell with best and worst data pattern is 8.6%. By comparing results from nominal and compact cell sizes with same data pattern, we observe a 3% variation at the 22 nm node.

2) Bulk Perpendicular MTJ: Fig. 14 exhibits Δ variation in CPMTJ. From the figure, CPMTJ also presents a decreasing trend of Δ variation as technology scales down and target Δ increases. However, the maximum variation in CPMTJ is less than maximum variation of IMTJ. From Fig. 9, we observe that magnitude of H_{stray} from PMTJ is less than IMTJ due to
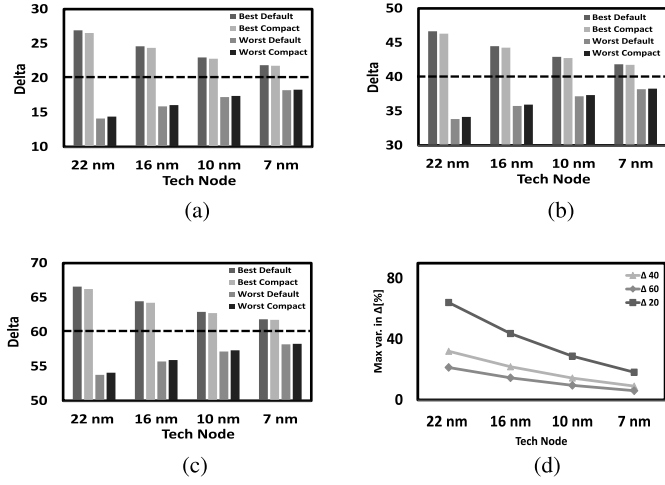
Fig. 14. Variation of Δ in CPMTJ with respect to technology nodes, data patterns, and cell array configuration. Variation with nominal (a) $\Delta = 20$, (b) $\Delta = 40$, and (c) $\Delta = 60$. (d) Maximum variation of Δ across combinations of data pattern and cell array configuration in technology node.
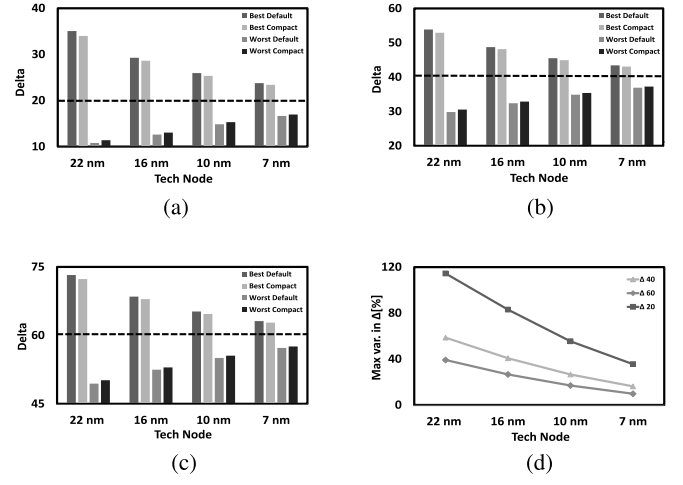

Fig. 16. Variation of Δ in IPMTJ with respect to technology nodes, data patterns, and cell array configuration. Variation with nominal (a) $\Delta = 20$, (b) $\Delta = 40$, and (c) $\Delta = 60$. (d) Maximum variation of Δ across combinations of data pattern and cell array configuration in technology node.
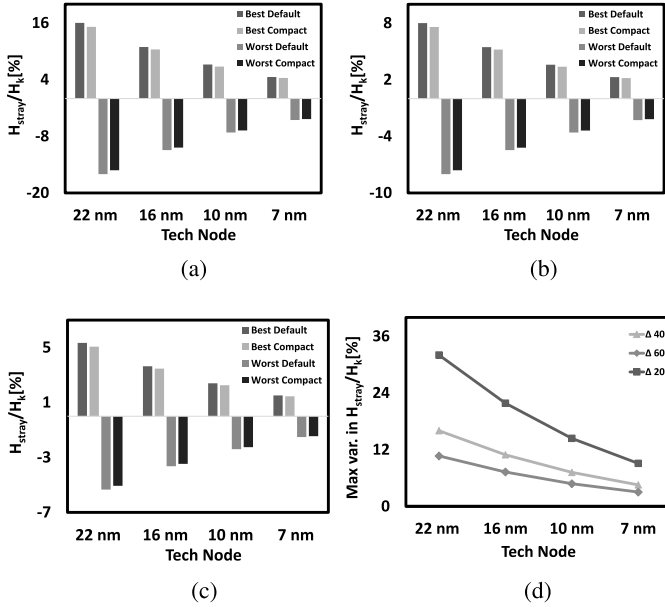

Fig. 15. Variation of H_{stray}/H_k in CPMTJ with respect to technology nodes, data patterns, and cell array configuration. Variation with nominal (a) $\Delta = 20$, (b) $\Delta = 40$, and (c) $\Delta = 60$. (d) Maximum variation of H_{stray}/H_k across combinations of data pattern and cell array configuration in technology node.
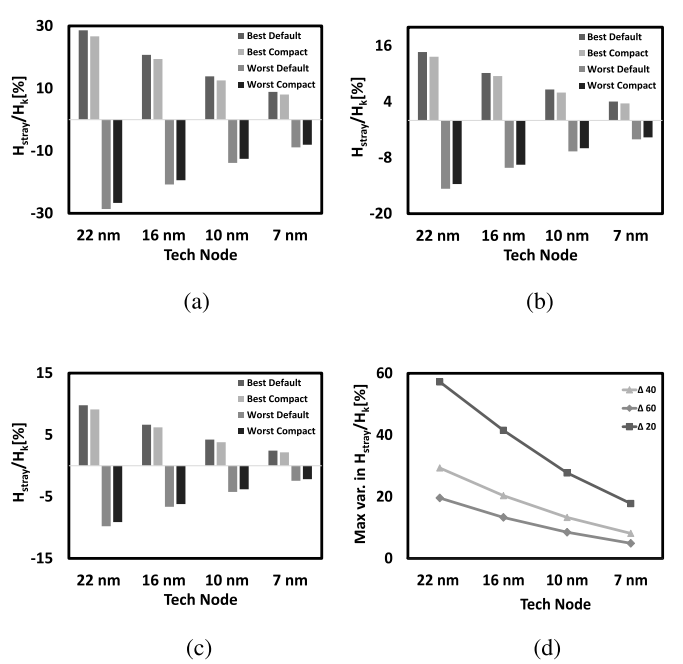

Fig. 17. Variation of H_{stray}/H_k in CPMTJ with respect to technology nodes, data patterns, and cell array configuration. Variation with nominal (a) $\Delta = 20$, (b) $\Delta = 40$, and (c) $\Delta = 60$. (d) Maximum variation of H_{stray}/H_k across combinations of data pattern and cell array configuration in technology node.

the geometry of MTJ types and the direction of M_s for the same magnitude of M_s. This result explains why (H_{stray}/H_k) across all technology node in PMTJ is less than that of IMTJ as shown in Fig. 15. As a result, we conclude that the Δ variation in PMTJ is less than that of IMTJ.

However, for CPMTJ the Δ variation in nominal and compact cell sizes is different from the Δ variation in IMTJ for different cell sizes. Between different cell sizes, maximum Δ variation is 2% in 22 nm at target $\Delta = 20$. From Biot–Savart law (4), magnetic field at a point is stronger when distance between a point and the current loop is closer. Therefore, in compact cells, each MTJs exerts more H_{stray} on the victim cell. Since M_s direction in IMTJ is in y-direction in 3 by 3

array, the sum of H_{stray} from neighboring cell at victim cell is larger when MTJs are compact. In the case of PMTJ, the sum of H_{stray} from neighboring MTJs on the victim cell decreases because the direction of M_s of MTJs is in the z-direction. When distance between neighboring and victim MTJs is too close, the direction of H_{stray} from neighboring cell deviate significantly, which results in less H_{stray} in the direction of M_s on victim cell.

3) Interface-Induced Perpendicular MTJ: Fig. 17 shows how (H_{stray}/H_k) changes across technology nodes, target Δ in different cell sizes and data patterns. Fig. 16 shows how
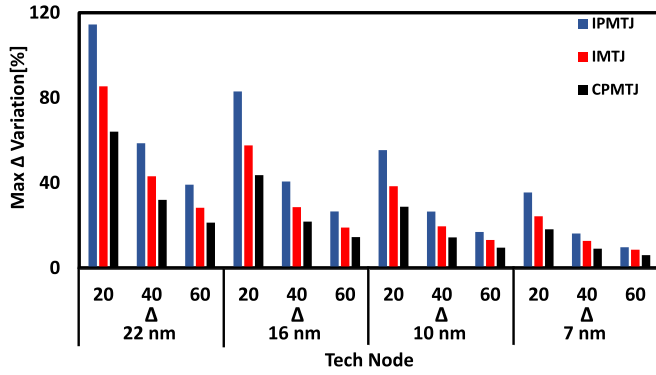
Fig. 18. Maximum variation of Δ in IMTJ, CPMTJ, and IPMTJ across combinations of data pattern and cell array configuration in technology node and nominal Δ.
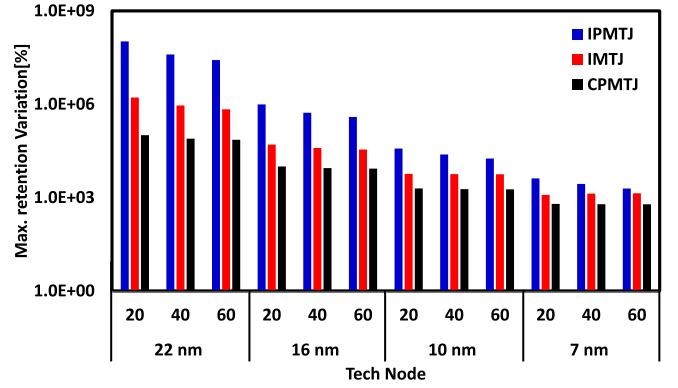

Fig. 19. Maximum variation of retention time in IMTJ, CPMTJ, and IPMTJ across combinations of data pattern and cell array configuration in technology node and nominal Δ.

much variation it caused in Δ. The effect of magnetic coupling on the Δ of IPMTJ is similar to that of CPMTJ. The only difference between IPMTJ and CPMTJ in terms of Δ variation is the magnitude of variation. The reason for this difference lies in the relationship between (2) and (5). For IMTJ and CPMTJ, as technology node scales, H_k is increased to compensate the loss in Δ caused by decreasing volume of MTJ. In IPMTJ, decreasing volume automatically increases H_k because decreasing t_f increases H_k. Therefore, H_k in IPMTJ is smaller than H_k in IMTJ and CPMTJ. It results in large variation in (H_{stray}/H_k) and Δ.

4) Comparison of the Effect of Magnetic Coupling on Δ Across MTJ Types: Fig. 18 summarizes the maximum Δ variation for IMTJ, CPMTJ, and IPMTJ across target Δ and technology nodes. As we discussed above, Δ variation due to magnetic coupling is in the order: IPMTJ, IMTJ, and CPMTJ. The conclusion from thermal stability analysis is that the Δ variation will not become a big problem as technology node decreases, which is counter intuitive. From intuition, we expect that magnetic coupling will become a severe problem as technology node scales because STT-MRAM array will become denser. However, if we allow for scaling laws and adjust H_k as technology node decreases, the effect of magnetic coupling on thermal stability diminishes, since the stray field is normalized by H_k. For the same reason, magnetic coupling has minimal effect when $\Delta = 60$ since H_k is higher than the H_k of MTJs with lower target Δ.

B. Effect of Magnetic Coupling on Retention Time

The average retention time (τ) of MTJ is exponentially dependent on the Δ [16]

$$\tau = \tau_0 \exp\left(\frac{K_u V}{k_B T}\right) = \tau_0 \exp(\Delta) \qquad (7)$$

where τ_0 is 1 ns. Since Δ is affected by magnetic coupling (6), the retention times for MTJ bits are affected as well. The loss of retention from the nominal retention time is exponential of the Δ variation and it exhibits the same trend as Δ variation in three MTJs.

Fig. 19 represents the maximum variation in retention across nominal Δ and technology nodes. Since the variation in retention is in exponential relationship with variation in Δ, the

variation tends to be very large in a cell with 22 nm and $\Delta = 20$ and it exhibits decreasing trend in retention variation as technology node decreases and nominal Δ increases.

V. EFFECT OF MAGNETIC COUPLING ON THE DYNAMIC PROPERTIES OF THE VICTIM CELL

In dynamic analysis, we explore how magnetic coupling causes variation in the critical current density (J_{c0}) and write times in IMTJ, CPMTJ, and IPMTJ.

A. Effect of Magnetic Coupling on Critical Current Density (J_{c0})

According to [26], the relation between magnetic coupling and J_{c0} in in-plane and PMTJ can be expressed as

$$\text{IPcell} J_{c0} = \frac{2e}{\hbar} \frac{\alpha}{\eta} (t M_s H_k)\left(1 + \frac{2\pi M_s}{H_k} + \frac{H_{\text{stray}}}{H_k}\right) \qquad (8)$$

$$\text{PPcell} J_{c0} = \frac{2e}{\hbar} \frac{\alpha}{\eta} (t M_s H_k)\left(1 + \frac{H_{\text{stray}}}{H_k}\right). \qquad (9)$$

(H_{stray}/H_k) is positive when H_{stray} is parallel to M_s and negative when it is anti-parallel. In other words, when H_{stray} is strong in the direction of M_s, the victim cell requires bigger J_{c0}. Therefore, the best case data pattern for Δ analysis becomes the worst case data pattern for J_{c0} consumption. For IMTJ, since the nominal cell size has weaker magnetic coupling than compact size cell, the nominal cell configuration reduces J_{c0} in IMTJ. For PMTJ, as we have observed from the static analysis, that the compact cell size reduces J_{c0} for PMTJ since it has weak magnetic coupling than the nominal cell. In this analysis, we set $\alpha = 0.01$ and $\eta = 0.81$ [16]. Fig. 20 shows how J_{c0} varies with technology node at different target Δ. IMTJ with nominal $\Delta = 60$ in 22 nm and 7 nm exhibits $J_{c0} = 9.1$ MA/cm^2 and 11.8 MA/cm^2. As technology node scales or the target Δ becomes larger, J_{c0} increases because H_k, as we have discussed in the previous section, increases. As we can see from [7], IMTJ shows slow increase in the rate of J_{c0} across technology nodes. The reason can be found from (8). Before scaling IMTJ, $(2\pi M_s/H_k)$ is a dominant component that decides J_{c0}. As we increase H_k to maintain Δ in scaled technology nodes, (H_{stray}/H_k) is marginally affected. Due to this reason, J_{c0} in IMTJ is does
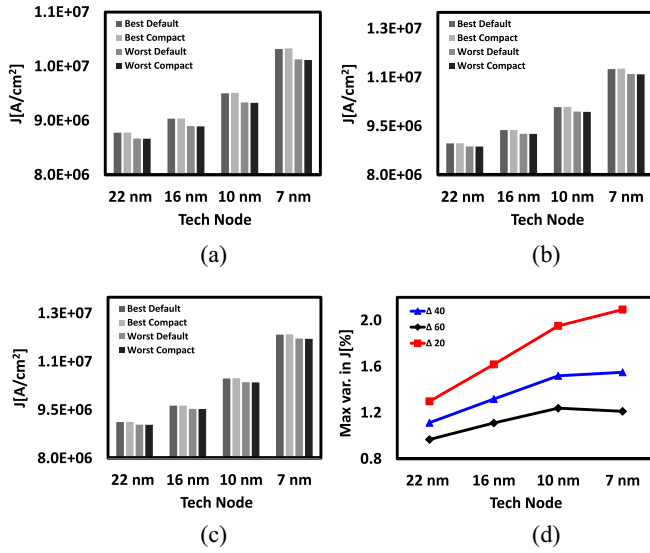
Fig. 20. Variation of J_{c0} in IMTJ with respect to technology nodes, data patterns, and cell array configuration. Variation with nominal (a) $\Delta = 20$, (b) $\Delta = 40$, and (c) $\Delta = 60$. (d) Maximum variation of J_{c0} across combinations of data pattern and cell array configuration in technology node.
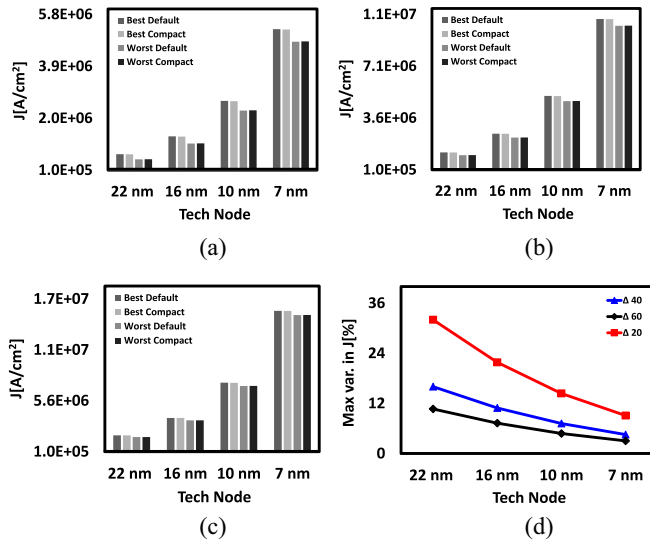

Fig. 21. Variation of J_{c0} in CPMTJ with respect to technology nodes, data patterns, and cell array configuration. Variation with nominal (a) $\Delta = 20$, (b) $\Delta = 40$, and (c) $\Delta = 60$. (d) Maximum variation of J_{c0} across combinations of data pattern and cell array configuration in technology node.

not increase significantly in lower technology nodes. For the same reason, a smaller variation in J_{c0} due to magnetic coupling across technology node, as shown in Fig. 20 can be explained.

Figs. 21 and 22 show how J_{c0} changes with magnetic coupling in CPMTJ and IPMTJ. Both MTJs show similar trend for J_{c0} as IMTJ with respect to technology node and nominal Δ. The main difference between IMTJ and PMTJ is the increasing rate in J_{c0} with technology scaling. As (9) shows, J_{c0} is directly proportional to H_k and J_{c0} increases rapidly as H_k increases to maintain same nominal Δ in lower technology node. For PMTJs in 22 nm, the J_{c0} with nominal $\Delta = 60$ is 1.78 MA/cm2. Because of the additional demagnetization field
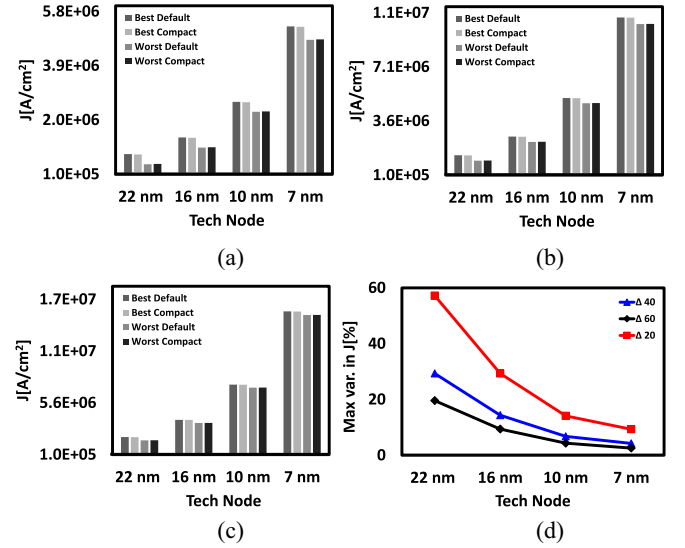

Fig. 22. Variation of J_{c0} in IPMTJ with respect to technology nodes, data patterns, and cell array configuration. Variation with nominal (a) $\Delta = 20$, (b) $\Delta = 40$, and (c) $\Delta = 60$. (d) Maximum variation of J_{c0} across combinations of data pattern and cell array configuration in technology node.

component, $(2\pi M_s/H_k)$ as shown in (8), the J_{c0} for IMTJ is greater than PMTJ [26]. However, as we scale down both IMTJ and PMTJ, we observe that J_{c0} in PMTJ become larger than J_{c0} of IMTJ since H_k in both CPMTJ and IPMTJ increases much faster than H_k in IMTJ. The variation in J_{c0} in CPMTJ due to magnetic coupling can become a significant challenge if nominal CPMTJ $\Delta = 20$ in 22 nm, as Fig. 21(d) indicates (32% variation). However, J_{c0} in CPMTJ with high nominal $\Delta = 60$ in 7 nm exhibits 3% variation. Due to large increase in H_k as we discussed above in advanced technology nodes, the variation term (H_{stray}/H_k) is reduced, which results in lower variation in J_{c0} in advanced technology node. As we observed earlier, Fig. 21(a)–(c) shows that compact cell configuration exhibits less deviation from nominal J_{c0} than the nominal cell configuration.

Similar to CPMTJ, J_{c0} variation due to magnetic coupling in IPMTJ shows sharp decrease as MTJ scales down, as shown in Fig. 22. As we can observe from Figs. 15 and 17, (H_{stray}/H_k) in IPMTJ is larger than CPMTJ (58% and 30% max variation in 22 nm) but they become almost equal as technology node scales down (20% and 12% max variation in 7 nm). Due to this reason, we conclude that the J_{c0} variation in IPMTJ is larger than CPMTJ at 22 nm and the maximum variation in J_{c0} for both CPMTJ and IPMTJ is 12% at 7 nm.

Fig. 23 is a summary for J_{c0} variation due to magnetic coupling in IMTJ, CPMTJ, and IPMTJ. From this figure, IMTJ and IPMTJ exhibits the lowest and highest variation in J_{c0}. This outcome is expected from static analysis since J_{c0} variation due to magnetic coupling is also proportional to (H_{stray}/H_k). As this figure and [7] show, both CPMTJ and IPMTJ exhibit sharp increase in J_{c0} as technology node scales down.

B. Effect of Magnetic Coupling on Write Times (t_{wr})

In order to analyze how magnetic coupling affects write time in MTJs, we used the macrospin model of the free
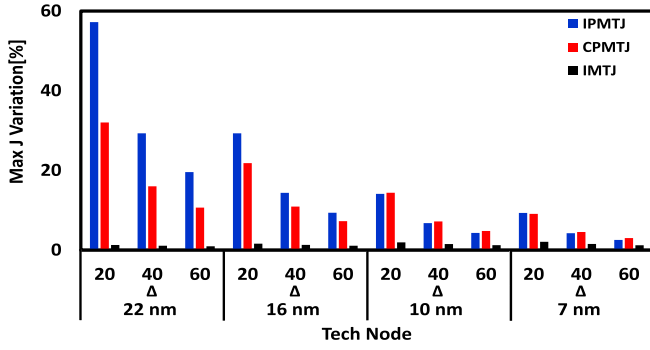
Fig. 23. Maximum variation of J_{c0} in IMTJ, CPMTJ, and IPMTJ across combinations of data pattern and cell array configuration in technology node and nominal Δ.
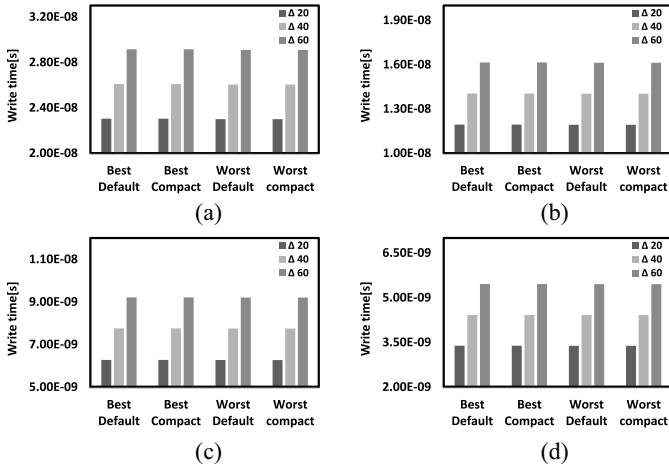

Fig. 24. Variation of write time in IMTJ when $I_{sw} = 600$ uA with respect to technology nodes, data patterns, and cell array configuration. Variation with nominal (a) $\Delta = 20$, (b) $\Delta = 40$, and (c) $\Delta = 60$. (d) Maximum variation of write time across combinations of data pattern and cell array configuration in technology node.

layer nanomagent and analyze the dynamics vis the Landau–Lifstitz–Gilbert (LLG) equation with an additional spin torque component [27], [28]. The equation below is the LLG equation with uniaxial anisotropy, easy-plane anisotropy, external magnetic field, and spin current torque terms [27], [28]

$$\frac{1+\alpha^2}{\gamma H_k}\begin{bmatrix}\frac{\partial\theta}{\partial t}\\[4pt]\frac{\partial\phi}{\partial t}\end{bmatrix} = \vec{T}_U + \vec{T}_K + \vec{T}_H + \vec{T}_S \tag{10}$$

$$\vec{T}_U = -\begin{bmatrix}\alpha\sin\theta\cos\theta\\ \cos\theta\end{bmatrix} \tag{11}$$

$$\vec{T}_K = -h_p\begin{bmatrix}(\sin\phi+\alpha\cos\theta\cos\phi)\sin\theta\cos\phi\\ (\cos\phi\cos\theta-\alpha\sin\phi)\cos\phi\end{bmatrix} \tag{12}$$

$$\vec{T}_H = -h\begin{bmatrix}\cos\phi\sin\psi+\alpha(\sin\theta\cos\psi-\cos\theta\sin\phi\sin\psi)\\ \sin\theta\cos\psi-\cos\theta\sin\phi\sin\psi-\alpha\cos\psi\sin\psi\\ \sin\theta\end{bmatrix} \tag{13}$$

$$\vec{T}_s = h_s\begin{bmatrix}-\sin\theta\\ \alpha\end{bmatrix}. \tag{14}$$

Here, the external magnetic field, $\vec{T}_H$, is caused by magnetic coupling and h is defined as (H_{stray}/H_k). In this analysis,
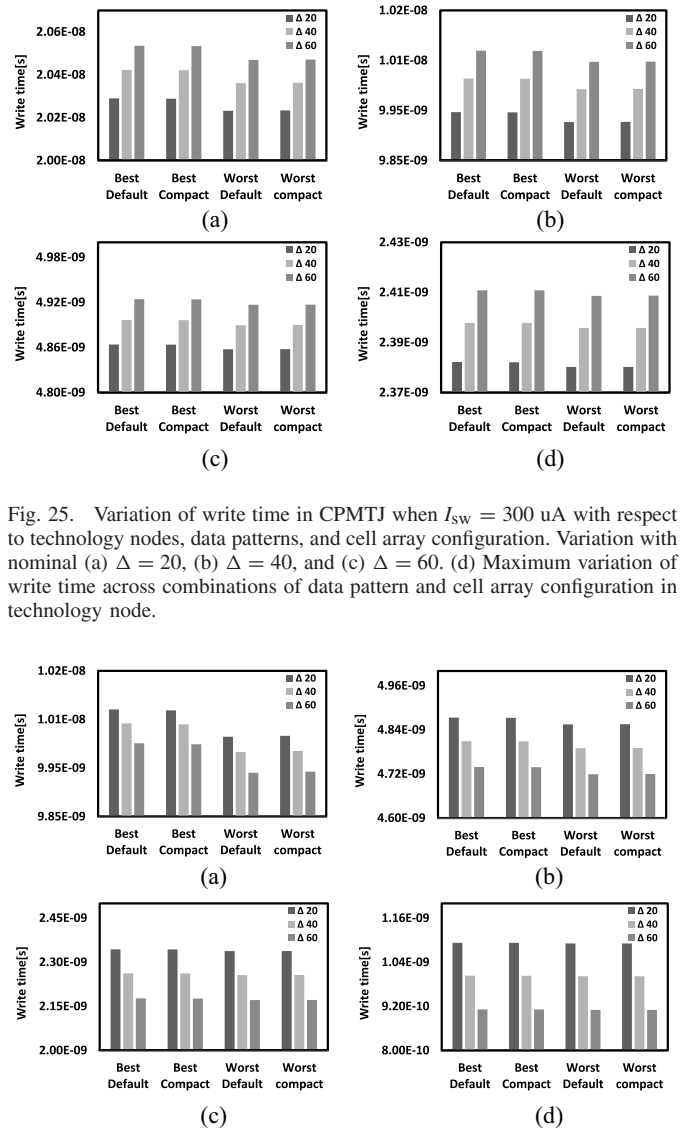

Fig. 25. Variation of write time in CPMTJ when $I_{sw} = 300$ uA with respect to technology nodes, data patterns, and cell array configuration. Variation with nominal (a) $\Delta = 20$, (b) $\Delta = 40$, and (c) $\Delta = 60$. (d) Maximum variation of write time across combinations of data pattern and cell array configuration in technology node.

Fig. 26. Variation of write time in IPMTJ when $I_{sw} = 300$ uA with respect to technology nodes, data patterns and cell array configuration. Variation with nominal (a) $\Delta = 20$, (b) $\Delta = 40$, and (c) $\Delta = 60$. (d) Maximum variation of write time across combinations of data pattern and cell array configuration in technology node.

we set hp, easy-plane anisotropy, term to 0 and we set $I_{sw} = 600$ uA for IMTJ and 300 uA for both CPMTJ and IPMTJ. After solving the nanomagnetic dynamics from the LLG equation, we measure the time for normalized M_z to reach from 1 to 0 to observe how write time changes with respect to technology node scaling and nominal Δ. From Figs. 24–26, we observe that write time of IMTJ with high Δ is larger than write time with low Δ. Also, we observe that write time decreases as technology node scales down. Since we increase H_k to maintain nominal Δ in scaled technology node, we tune the material parameters through retargetting of $[(1+\alpha^2)/\gamma H_k]$. Equation (10), which results in lower write time as the technology node scales down.

We observe from Fig. 27, that the variation due to magnetic coupling in write time is not significant compared to the variation in Δ and J_{c0}. In order to maintain thermal stability across
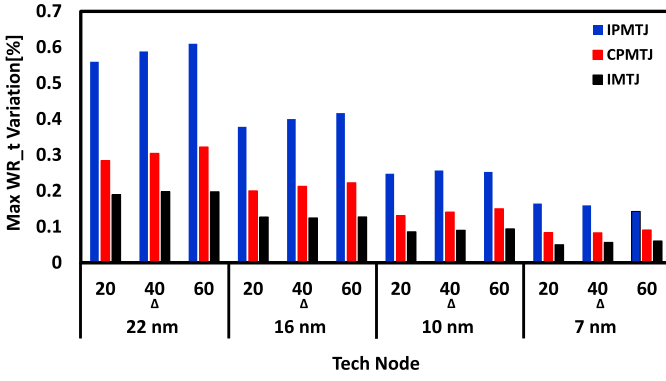
Fig. 27. Maximum variation of write time in IMTJ, CPMTJ, and IPMTJ across combinations of data pattern and cell array configuration in technology node and nominal Δ.

Fig. 28. H/H_k sensitivity analysis with respect to x an y-axis space between cells in array, AR, K_u, and t_f in 22 nm, nominal $\Delta = 60$. Maximum variation in (a) H/H_k of each MTJ types with respect to variation of cell spacing in x-axis, (b) H/H_k of each MTJ types with respect to variation of cell spacing in y-axis, and (c) H/H_k of each MTJ types with respect to variation of AR in IMTJ, K_u in CPMTJ and t_f in IPMTJ.

different technology nodes, one needs to scale up H_k. This can be done by designing the nanomagnet for higher shape or interfacial anisotropy. We observe that the main reason why the variance of thermal stability due to stray field H is not reflected in the write time is due to the term $[(1 + \alpha^2)/\gamma H_k]$ from the LLG equation. The term scales the effect of stray field in write time. Since with scaling H_k increases, the overall effect on write dynamics decreases due to the scaling of $[(1 + \alpha^2)/\gamma H_k]$.

Even before technology node scaling, IPMTJ with nominal $\Delta = 60$ shows 0.6% variation in write time and as technology node scales down, the variation reduces to less than 0.1%. Magnetic coupling causes most variation in write time in IPMTJ and the least in IMTJ. In summary, write time variation due to magnetic coupling is not a significant problem and is expected to remain insignificant as MTJ scales down.

VI. SENSITIVITY OF THE STRENGTH OF MAGNETIC COUPLING TO PROCESS VARIATIONS

In this section, we explore how H/H_k in IMTJ, CPMTJ, and IPMTJ are affected by the coupling magnetic field under process induced variations. Both the planar dimensions of the MTJs are varied as they contribute to changes in H_{stray} on the victim node. Also, for each cell types, we vary the AR for the IMTJ, K_u for CPMTJ and t_f for IPMTJ as these design parameters affect H_k. This in turn affects the role of H_{stray} on the electrical characteristics of the bit cell.

Fig. 28 illustrates the sensitivity of H/H_k to the five design parameters mentioned above for all the MTJ types in 22 nm with $\Delta = 60$. From Fig. 28(a) and (b), we can see that even 20% variation in x and y spacing in cell size does not significantly affect H/H_k. However, from Fig. 28(c), 8% variation in AR and K_u in IMTJ and CPMTJ causes more than 15% variation in H/H_k and 4% variation in t_f in IPMTJ causes more than 250% variation in H/H_k.

Figs. 29 and 30 represent the maximum H/H_k variation across technology nodes while varying xsp, ysp by 40%, AR, K_u by 8% and t_f by 4%. As technology node scales down, we observe that H/H_k variation caused by x-axis spacing and y-axis spacing increases in all MTJ types. According to Fig. 29, IMTJ is most susceptible to x and y-axes spacing
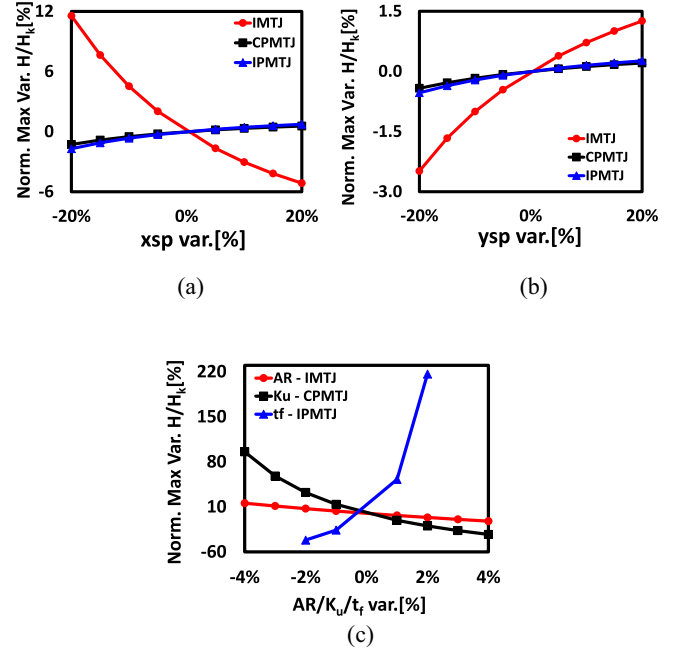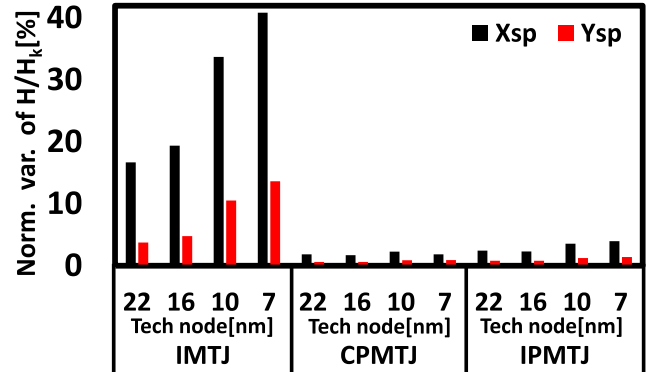

Fig. 29. Maximum variation of H/H_k in IMTJ, CPMTJ, and IPMTJ with respect to -20% to 20% variation of x-axis and y-axis spacing between cells in an array.

variation and PMTJs exhibit minimum variation in H/H_k. In Fig. 30, variation in AR in different technology nodes exhibit almost the same variation in H/H_k for IMTJ. On the other hand, variation of K_u and t_f in CPMTJ and IPMTJ show that H/H_k variation decreases as technology node scales down.

VII. MAGNETIC COUPLING EFFECT ON THERMAL STABILITY WITH SYNTHETIC ANTI-FERROMAGNET FIXED LAYER

So far, we have explored the effects of magnetic coupling on static and dynamic characteristics of STT-MRAM under the assumption that the fixed layer of MTJs are ferromagnets and exert magnetic fields in their neighborhood. Therefore,
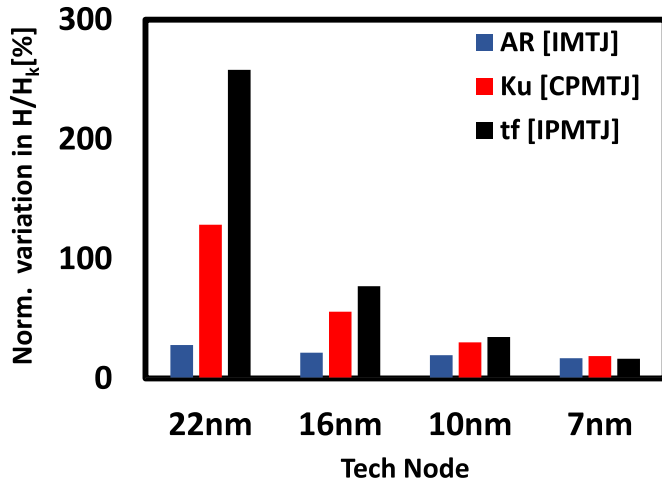
Fig. 30. Maximum variation of H/H_k in IMTJ, CPMTJ, and IPMTJ with respect to variation of AR in IMTJ, K_u in CPMTJ, and t_f in IPMTJ.
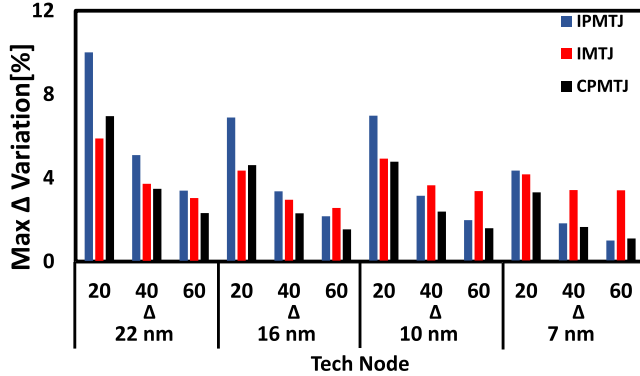

Fig. 31. Maximum variation of Δ in IMTJ, CPMTJ, and IPMTJ across combinations of data pattern and cell array configuration in technology node and nominal Δ.

large portion of external magnetic field exerted on the victim cell is emanated from fixed layers of MTJs in adjacent cells. However, when fixed layer of an MTJ is a synthetic anti-ferromagnet, i.e., the magnetic field lines from the fixed layer will close on itself, the results of the same analysis is expected to be very different. In order to compare the results, we model the interaction of STT-MRAM bit-cells without any magnetic field contribution from the fixed layer. We observe that the variation in thermal stability across different technology nodes and cell sizes reduce significantly but they are still not negligible in scaled nodes.

Fig. 31 shows the maximum variation of thermal stability in IMTJ, CPMTJ, and IPMTJ across various data patterns. The variation has decreased to approximately (1/10)th of what we observed in Fig. 18. Since, the variation in J_{c0} and t_{wr} of a cell exhibit less variation compared to thermal stability variation, we can deduce that the variation in J_{c0} and t_{wr} is greatly reduced when fixed layer of an MTJ does not exert any magnetic field on this neighbors. However, given the exponential relationship between Δ and the retention time, care must be taken when data is stored in the STT-MRAM array over long periods of time.

VIII. Conclusion

In this paper, we present a model of magnetic field induced coupling between adjacent bits in an STT-MRAM array. A comprehensive analysis, across four technology nodes and different MTJ technologies has been presented. We have analyzed the role of the magnetic coupling on electrical performance, both static and dynamic. We conclude that for MTJ technologies with dense memory bits and lower stored energy, the coupling field can cause significant change in the average retention time. Data patterns that activate the worst and best case scenarios have also been explored. Dynamic analysis reveals that write times and critical current densities are weakly disturbed by the coupling field. Finally, the sensitivity of the coupling field on process induced variation has been reported. It should be noted that this paper explores ultra-dense memory bit cells with cell sizes which are $15F^2$ and $6F^2$. Raychowdhury et al. [29], the state-of-the art bit-cells are significantly larger ($2\times$ to $3\times$ larger) and effects, such as magnetic coupling will be reduced. However, key observations, such as the data pattern dependence of retention, will remain unchanged and as the technology matures and denser bit-cells are enabled, magnetic field induced coupling will play a key role in both design and test.

References

[1] Y. Huai, "Spin-transfer torque MRAM (STT-MRAM): Challenges and prospects," *AAPPS Bull.*, vol. 18, no. 6, pp. 33–40, 2008.
[2] A. Fert, "Origin, development, and future of spintronics (Nobel lecture)," *Angewandte Chem. Int. Edition*, vol. 47, no. 32, pp. 5956–5967, 2008.
[3] C. Chappert, A. Fert, and F. N. Van Dau, "The emergence of spin electronics in data storage," *Nat. Mater.*, vol. 6, no. 11, pp. 813–823, 2007.
[4] C. Augustine et al., "Numerical analysis of typical STT-MTJ stacks for 1T-1R memory arrays," in *Proc. IEEE Int. Electron Devices Meeting (IEDM)*, San Francisco, CA, USA, 2010, p. 22.
[5] K. C. Chun et al., "A scaling roadmap and performance evaluation of in-plane and perpendicular MTJ based STT-MRAMs for high-density cache memory," *IEEE J. Solid-State Circuits*, vol. 48, no. 2, pp. 598–610, Feb. 2013.
[6] Y. Chen et al., "Design margin exploration of spin-transfer torque RAM (STT-RAM) in scaled technologies," *IEEE Trans. Very Large Scale Integr. (VLSI) Syst.*, vol. 18, no. 12, pp. 1724–1734, Dec. 2010.
[7] J. Kim et al., "A technology-agnostic MTJ SPICE model with user-defined dimensions for STT-MRAM scalability studies," in *Proc. IEEE Custom Integr. Circuits Conf. (CICC)* vol. 1. San Jose, CA, USA, 2015, pp. 1–4.
[8] J. Kim et al., "Scaling analysis of in-plane and perpendicular anisotropy magnetic tunnel junctions using a physics-based model," in *Proc. 72nd Annu. Device Res. Conf. (DRC)*, Santa Barbara, CA, USA, 2014, pp. 155–156.
[9] E. Chen et al., "Advances and future prospects of spin-transfer torque random access memory," *IEEE Trans. Magn.*, vol. 46, no. 6, pp. 1873–1878, Jun. 2010.
[10] J.-H. Park et al., "Enhancement of data retention and write current scaling for sub-20nm STT-MRAM by utilizing dual interfaces for perpendicular magnetic anisotropy," in *Dig. Tech. Papers Symp. VLSI Technol.*, vol. 721. Honolulu, HI, USA, 2012, pp. 57–58.
[11] W. Kim et al., "Extended scalability of perpendicular STT-MRAM towards sub-20nm MTJ node," in *Tech. Dig. Int. Electron Devices Meeting (IEDM)*, Washington, DC, USA, 2011, pp. 1–4.

[12] A. Raychowdhury, D. Somasekhar, T. Karnik, and V. De, "Design space and scalability exploration of 1T-1STT MTJ memory arrays in the presence of variability and disturbances," in *Proc. IEEE Int. Electron Devices Meeting (IEDM)*, Baltimore, MD, USA, 2009, pp. 1–4.

[13] M. Hosomi *et al.*, "A novel nonvolatile memory with spin torque transfer magnetization switching: Spin-RAM," in *IEEE Int. Electron Devices Meeting (IEDM) Tech. Dig.*, Washington, DC, USA, 2005, pp. 459–462.

[14] S. Ikeda *et al.*, "A perpendicular-anisotropy CoFeB-MgO magnetic tunnel junction," *Nat. Mater.*, vol. 9, no. 9, pp. 721–724, 2010.

[15] H. Sato *et al.*, "Comprehensive study of CoFeB-MgO magnetic tunnel junction characteristics with single- and double-interface scaling down to 1X nm," in *Proc. IEEE Int. Electron Devices Meeting (IEDM)*, Washington, DC, USA, 2013, pp. 1–4.

[16] A. V. Khvalkovskiy *et al.*, "Erratum: Basic principles of STT-MRAM cell operation in memory arrays," *J. Phys. D Appl. Phys.*, vol. 46, no. 13, 2013, Art. no. 139601.

[17] S. Yuasa *et al.*, "Future prospects of MRAM technologies," in *Proc. IEEE Int. Electron Devices Meeting (IEDM)*, vol. 2. Washington, DC, USA, 2013, pp. 1–4.

[18] Y. Zhang, W. Wen, and Y. Chen, "The prospect of STT-RAM scaling from readability perspective," *IEEE Trans. Magn.*, vol. 48, no. 11, pp. 3035–3038, Nov. 2012.

[19] W. H. Choi, J. Kim, I. Ahmed, and C. H. Kim, "Comprehensive study on interface perpendicular MTJ variability," in *Proc. Device Res. Conf.*, Columbus, OH, USA, 2015, pp. 89–90.

[20] D. J. Griffiths, *Introduction to Electrodynamics*, 4th ed. San Francisco, CA, USA, Pearson, 2012.

[21] W. Kang *et al.*, "Reconfigurable codesign of STT-MRAM under process variations in deeply scaled technology," *IEEE Trans. Electron Devices*, vol. 62, no. 6, pp. 1769–1777, Jun. 2015.

[22] W. Kang *et al.*, "Yield and reliability improvement techniques for emerging nonvolatile STT-MRAM," *IEEE J. Emerg. Sel. Topic Circuits Syst.*, vol. 5, no. 1, pp. 28–39, Mar. 2015.

[23] I. Yoon, A. Chintaluri, and A. Raychowdhury, "EMACS: Efficient MBIST architecture for test and characterization of STT-MRAM arrays," in *Proc. Int. Test Conf.*, Fort Worth, TX, USA, 2016, pp. 1–10.

[24] A. J. Van de Goor and I. B. S. Tlili, "Disturb neighborhood pattern sensitive fault," in *Proc. 15th IEEE VLSI Test Symp. (VTS)*, Monterey, CA, USA, Apr./May 1997, pp. 37–45.

[25] T. Kawahara, K. Ito, R. Takemura, and H. Ohno, "Spin-transfer torque RAM technology: Review and prospect," *Microelectron. Rel.*, vol. 52, no. 4, pp. 613–627, 2012.

[26] A. V. Khvalkovskiy *et al.*, "Basic principles of STT-MRAM cell operation in memory arrays," *J. Phys. D Appl. Phys.*, vol. 46, no. 7, 2013, Art. no. 074001.

[27] J. Z. Sun, "Spin-current interaction with a monodomain magnetic body: A model study," *Phys. Rev. B, Condens. Matter*, vol. 62, no. 1, pp. 570–578, 2000.

[28] G. D. Panagopoulos, C. Augustine, and K. Roy, "Physics-based SPICE-compatible compact model for simulating hybrid MTJ/CMOS circuits," *IEEE Trans. Electron Devices*, vol. 60, no. 9, pp. 2808–2814, Sep. 2013.

[29] A. Raychowdhury, D. Somasekhar, T. Karnik, and V. De, "Design space and scalability exploration of 1T-1STT MTJ memory arrays in the presence of variability and disturbances," in *Proc. IEEE Int. Electron Devices Meeting (IEDM)*, Baltimore, MD, USA, 2009, pp. 1–4.

Insik Yoon (S'17) received the B.S. and M.S. degrees from Carnegie Mellon University, Pittsburgh, PA, USA, in 2009 and 2010, respectively. He is currently pursuing the Ph.D. degree with the Georgia Institute of Technology, Atlanta, GA, USA.

From 2010 to 2015, he was with Memory and Display Interface Design, TLi and SK Hynix, Icheon, South Korea. His current research interests include emerging memory technologies and hardware implementation for cryptography.

Arijit Raychowdhury (M'07–SM'13) received the Ph.D. degree in electrical and computer engineering from Purdue University, West Lafayette, IN, USA, in 2007.

He joined the Georgia Institute of Technology, Atlanta, GA, USA, in 2013, where he is an Associate Professor with the School of Electrical and Computer Engineering, and currently holds the ON Semiconductor Junior Professorship. His industry experience includes five years as a Staff Scientist with Circuits Research Laboratory, Intel Corporation, Santa Clara, CA, USA, and a year as an Analog Circuit Researcher with Texas Instruments Inc., Dallas, TX, USA. He holds over 25 U.S. and international patents and has published over 100 articles in journals and refereed conferences. His current research interests include low power digital and mixed-signal circuit design, device-circuit interactions and novel computing models, and hardware realizations.

Dr. Raychowdhury was a recipient of the Intel Early Faculty Award in 2015, the NSF CISE Research Initiation Initiative Award (CRII) in 2015, the Intel Labs Technical Contribution Award in 2011, the Dimitris N. Chorafas Award for Outstanding Doctoral Research in 2007, the Best Thesis Award, College of Engineering, Purdue University in 2007, and the multiple best paper Awards and Fellowships.